

Contents:

- S1) The Orbital Dynamics Calculations.
- S2) Collisional and Dynamical Depletion Evolution Model (CoDDEM) Calculations.
- S3) The Micrometeorite Origin Problem.
- S4) The Collisional Evolution of the Primordial Cometary Disk.

S1. The Orbital Dynamics Calculations

The goal of these simulations is to follow the long-term orbital evolution of a large number of massless test particles (which represent primitive objects originally from the distant proto-planetary disk) under the gravitational influence of the giant planets. Initially the orbits of the planets change (sometimes violently), but they eventually settle into their current configuration.

The first step models the evolution of the system during the time when the gas giant planets migrate and primitive bodies are injected into the Jupiter-Saturn region by Uranus and Neptune as they penetrate the primitive planetesimal disk. Because Uranus and Neptune are far from the Sun (beyond ~ 15 AU) and we are interested in the dynamical evolution of objects in the ~ 2 to ~ 5 AU zone, we only include Jupiter and Saturn in the simulations. As the Nice model specifies, these planets start slightly interior to the 1:2 mean motion resonance (MMR) with one another. They were forced to migrate by including a suitably chosen acceleration term in the planets equations of motion. In particular, we chose an evolution similar to the ‘fast migration’ run in Ref. [3]. In these simulations, however, we took increased care to reproduce the observed eccentricities of the giant planets and the period of the Great Inequality at the end of the simulation. The temporal evolution of the planetary orbits employed in our simulations is shown in Fig. 1.

We followed the system for 10 million years using the SyMBA orbital integrator [31]. We removed a disk particle if it either impacted a planet, or reached a heliocentric distance greater than 15 AU or less than 1.5 AU (i.e. became Mars-crossing). We added the last requirement to account for the terrestrial planets, which were not directly included in the simulations. Every time that a test particle was dynamically eliminated, it was reintroduced on its original trans-Saturnian orbit rescaled to the current position of Saturn. Thus, we supplied a steady flux of planetesimals through the Jupiter-Saturn system during the entire integration. In this way, the number of particles in the simulation at any time was held constant at 834,500. In total ~ 31 million disk particles were eliminated and reintroduced during the considered time-span. At the

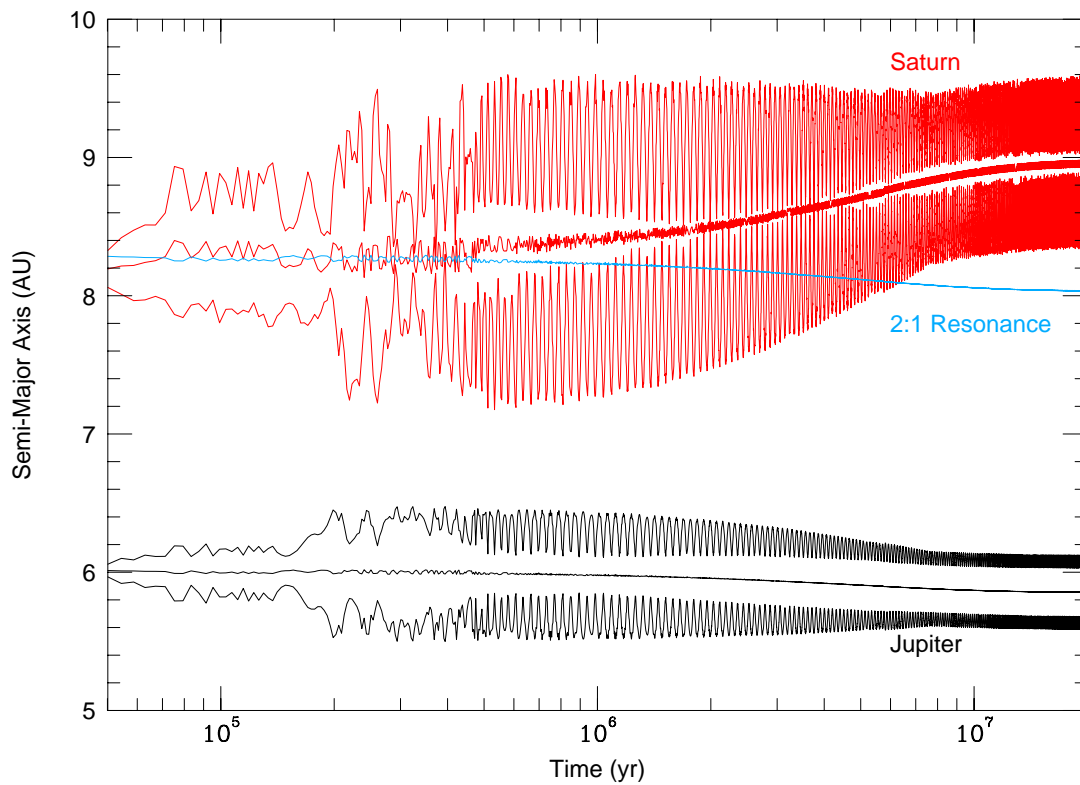


Fig. 1.— The black curves show the temporal evolution of the perihelion distance, semi-major axes and aphelion distance of Jupiter (from bottom to top, respectively) in the first stage of our dynamical simulations. The red curves are the same for Saturn. The blue curve shows the location of the 1:2 MMR with Jupiter. The system starts with Jupiter and Saturn interior to this resonance, but since the planets diverge, they soon cross it. According to the Nice model this resonance crossing triggers an instability in the ice giant orbits, which, in turn, scatters primitive planetesimals throughout the planetary system. A small fraction of these objects are then captured into the Hilda, Trojan, and OMB regions.

end of the 10 Myr simulation, there were 1147 particles captured onto orbits that were isolated from encounters with the planets.

Next, we determined the long-term stability of the particles captured during the migration simulations by integrating the system from 10^7 to 4×10^9 years using the integrator of Ref. [32] with a timestep of 0.1 yr. We removed any particle that impacted a planet, became Mars-crossing, reached a heliocentric distance of 15 AU, or entered a planet's Hill's sphere. Fig. 2 shows the number of test bodies in the long-term simulations as a function of time. Initially, there were 1147 particles — 218 were Trojans, 196 were Hildas, and 395 were in the OMB. At the end of 4 billion years of dynamical evolution there were 32 Trojans, 19 Hildas, and 158 OMB particles remaining. Note that these numbers do not include the effects of collisional grinding.

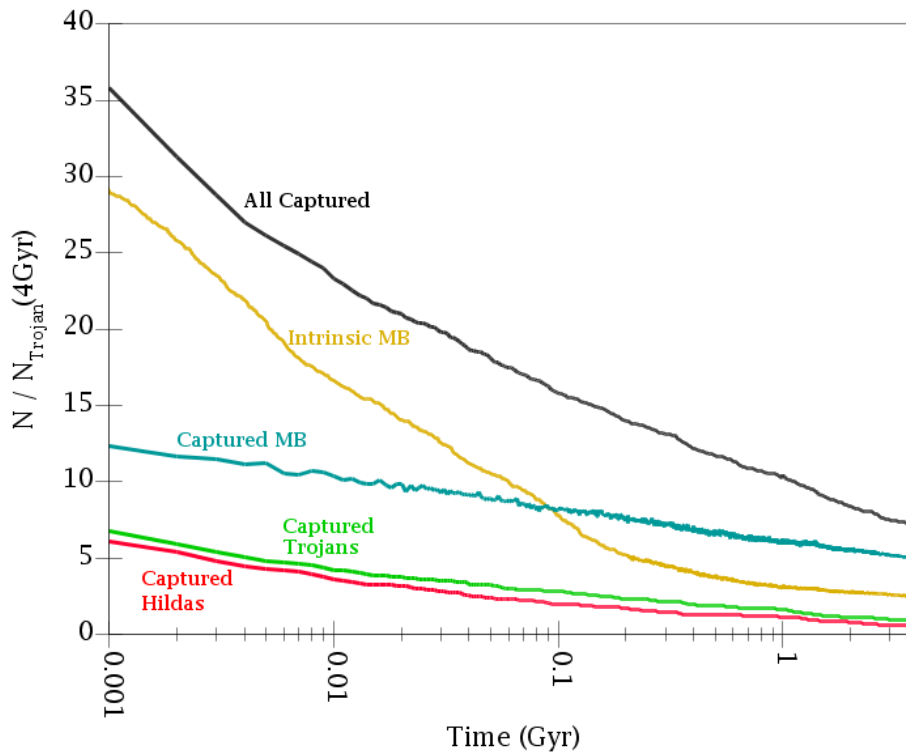


Fig. 2.— The temporal evolution of the number of objects in our long-term dynamical simulations scaled to the number of model Trojans that survived to the current epoch. The black curve shows all the captured objects, while the red, blue, and green curves show the three main captured populations in the Hilda, Trojans, and the main asteroid belt regions, respectively. The tan curve shows the temporal evolution of the indigenous main belt as described in §S2.1.

S2. Collisional and Dynamical Depletion Evolution Model (CoDDEM) Calculations

The size-frequency distribution (SFD) evolution results described in the main text were computed using the 1-dimension collisional and dynamical depletion evolution model called CoDDEM [13, 14]. CoDDEM was modified to use a more modern and complete algorithm for calculating the outcomes of collisions developed by Ref. [15], which, in turn, was based on 160 impact experiments performed using smooth particle hydrodynamic (SPH) codes coupled with N -body codes [33, 34]. In these runs, Ref. [33, 34] tracked $D = 10$ -46 km projectiles slamming into $D = 100$ km basaltic spheres at a wide range of impact speeds (2.5-7 km/s) and impact angles (15° - 75°). In addition, CoDDEM now includes the effects of cratering events.

Using CoDDEM, we tracked the evolution of 5 independent populations: (1) indigenous inner main belt (IMB), (2) indigenous outer main belt (I-OMB), (3) captured outer main belt (C-OMB), (4) Hildas, and (5) Trojans. Each of the above populations is represented by several parameters in the code: i) the SFD, ii) the collision probabilities, iii) the impact velocities, iv) the bulk densities, and v) the disruption scaling law. The code follows the evolution of the SFD while holding the rest

of the parameters constant.

In addition, each population was forced to decay over time due to the dynamical effects described in §S1 and in the main text. Note that we follow the collisional evolution of the system only after the first 10 Myr, i.e. after migration is over. Thus, we are assuming that collisional grinding is not important during the implantation process. We believe that this is reasonable because the dynamical lifetime of particles once they cross the orbit of Saturn is very short, $\sim 10^5$ yrs, and thus, there is not really much time for collisional evolution to occur. Indeed, there is observational evidence to this effect in the fact that the size-distributions of the Trojans and the cold classical Kuiper belt are similar [35].

We now discuss the initial values of the parameters for each of our populations. In particular, we discuss the indigenous and captured populations separately.

S2.1 Indigenous Main Belt Populations

Here we describe the indigenous main belt populations 1 (IMB) and 2 (I-OMB) used in our simulations. The IMB is defined as the collection of objects with $2.1 \leq a < 2.82$ AU, while the OMB is defined as those objects with $2.82 \leq a < 3.27$ AU.

Collision probabilities and impact velocities. To quantify the collision probabilities and impact velocities of populations in the main belt region striking either each other or the Hilda population (the main belt does not collide with the Trojans) we used the techniques and code described in Ref. [36], which computes the average “intrinsic collision probability” P_i and mean impact velocity V_{imp} for any two populations based on the semi-major axes, eccentricities and inclinations of their members. We represented the IMB and both the OMB populations using the 270 and 412 known asteroids, respectively, with $D > 50$ km. For the Hildas, we chose the 110 known asteroids with $H < 12$, which is likely close to a observationally complete set of objects. The values of P_i and V_{imp} derived from these calculations are found in Tables 1 and 2.

Population:	1	2	3	4	5
	IMB	I-OMB	C-OMB	Hildas	Trojans
1	4.9×10^{-18}	2.3×10^{-18}	2.3×10^{-18}	2.6×10^{-19}	0
2	2.3×10^{-18}	2.8×10^{-18}	2.8×10^{-18}	9.1×10^{-19}	0
3	2.3×10^{-18}	2.8×10^{-18}	2.8×10^{-18}	9.1×10^{-19}	0
4	2.6×10^{-19}	9.1×10^{-19}	9.1×10^{-19}	2.3×10^{-18}	2.4×10^{-19}
5	0	0	0	2.4×10^{-19}	3.0×10^{-18}

Table 1: The intrinsic impact probability (P_i) of the target population being struck by the impactor population. These numbers are in units of $\text{km}^{-2} \text{yr}^{-1}$. Note that this matrix is symmetric, as it should be.

Population:	1	2	3	4	5
	IMB	I-OMB	C-OMB	Hildas	Trojans
1	5.6	5.4	5.4	5.7	—
2	5.4	5.3	5.3	4.7	—
3	5.4	5.3	5.3	4.7	—
4	5.7	4.7	4.7	3.1	4.6
5	—	—	—	4.6	5.2

Table 2: The impact velocity (V_{imp}) in units of km/s. Note that this matrix is symmetric, as expected.

Bulk densities. As a simplifying approximation, we assumed the indigenous asteroids have a mean bulk density of 2.7 g cm^{-3} [37].

Catastrophic disruption scaling law (Q_D^).* The function Q_D^* , the critical impact specific energy, is defined as the energy per unit target mass needed to disrupt the target and send 50% of its mass away at escape velocity. For the IMB and I-OMB populations, we used a Q_D^* function derived by Ref. [13, 14] using CoDDEM; it is shown as the blue curve in Fig. 3.

Dynamical Evolution. The Nice model simulations [4] show that the dynamical evolution of the indigenous populations (i.e. IMB and I-OMB) is strongly dependent on the dynamical state of the asteroid belt at the time of the instability. Unfortunately, we have very few constraints on this issue. Thus, we adopted the asteroid belt simulation from Ref. [4] that best reproduced the characteristics of the LHB on the Moon. The Ref. [4] calculations only lasted for 200 Myr, and so we extended the one employed here to 4 Gyr. The dynamical depletion of the indigenous asteroid belt according to this model is shown in as the tan curve in Fig. 2. We find that 92% of the population becomes unstable in 4 Gyr, with half leaving in the first ~ 6 My after the giant planet instability.

Size-frequency distributions. In order to select starting SFDs for the inner and outer main belt, we first had to estimate their current SFDs. We follow the same procedures given below for both populations.

Our estimates are derived from the population of all known small bodies from the Minor Planet Center via the “astorb.dat” database computed by Edward Bowell (see <ftp://ftp.lowell.edu/pub/elgb/astorb.html>) with perihelion $q > 1.66 \text{ AU}$, and $2.1 \leq a < 2.82 \text{ AU}$ for the IMB and $2.82 \leq a < 3.27 \text{ AU}$ for OMB. We calculated the diameter (D) of each object from their published absolute magnitudes (H) assuming a geometric albedo, p_V (e.g., Ref. [38, 39]). In particular, in order to account for the fact that p_V varies within the MB, we assumed that bodies in $2.1 < a < 2.5 \text{ AU}$, $2.5 < a < 2.82 \text{ AU}$, and $2.82 < a < 3.27 \text{ AU}$ regions had p_V values of 0.18, 0.13, and 0.09, respectively. These data were used to construct the two SFDs for $D > 2 \text{ km}$. The shape of the SFDs for $D < 2 \text{ km}$, where the “astorb.dat” database is observationally incomplete,

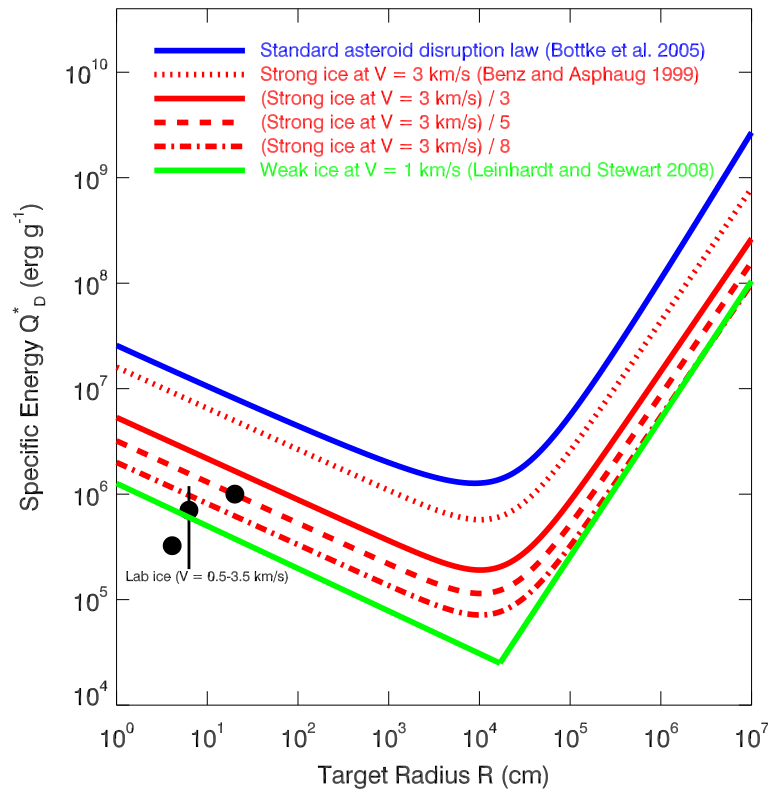


Fig. 3.— The disruption scaling law Q_D^* functions described in the text. We define the function Q_D^* , the critical specific impact energy, as the energy per unit target mass needed to disrupt the target and eject 50% of its mass. The blue curve shows the standard disruption function for asteroids derived by Ref. [13, 14]. The green curve shows the minimum value for weak ice as determined from numerical CTH impact experiments, while the black dots are data from laboratory disruption experiments into weak nonporous ice [19]. The dotted red curve is data from numerical SPH impact experiments on ice targets using a strong formulation for ice ([20]; see also Ref. [19]). This is our standard $f_Q = 1$ function. Finally, the solid, dashed, and dot-dashed red curves show $f_Q = 3, 5,$ and $8,$ respectively. Note that our calculations are performed for $R > 0.1$ km and thus they are mainly in the regime where the self-gravity of the target dominates the outcome of the collision (i.e. the regions where the slopes of the curves are positive) rather than its physical strength.

was assumed to follow that of Ref. [13, 14].

Using insights gleaned from main belt evolution models [13, 14] as well as studies of the ancient cratered terrains of the Moon, Mercury, and Mars [40], we argue that the shape of the indigenous main belt SFD has experienced minimal changes since the end of the late heavy bombardment ~ 4 Gy ago. However, to correct for a modest amount of collisional erosion, the starting IMB and I-OMB populations in our CoDDEM runs were increased by a small factor (1.1) in addition to what is required for the dynamical depletion (cf. tan curve in Fig.2).

S2.2 Captured Population

The parameters needed to model the captured main belt population (C-OMB; population 3), the Hildas (population 4), and the Trojans (population 5) are given below.

Collision probabilities and impact velocities. Calculating the impact parameters for resonant populations is complicated because the orientation of their orbits are correlated. Fortunately, these parameters for Hilda-Hilda, Trojan-Trojan, Hilda-Trojan collisions were calculated by Ref. [41]. To calculate the collision parameters between either the Hildas (population 4) or Trojans (population 5) and populations 1–3, we used the techniques described in §2.1. All these values are found in Tables 1 and 2.

Bulk densities. The bulk densities (ρ) of objects in the C-OMB, Hilda, and Trojan populations are largely unknown. Assuming these objects all came from the primordial trans-planetary belt, we can glean insights into their representative bulk densities by studying the available density information that exists for Trojans and Kuiper-Belt objects. A survey of the literature produces values of between 0.46 (Centaur 2002 CR₄₆ [42]) and 2.5 g cm⁻³ (Binary Trojan (624) Hektor [43]). Based on this data, we assumed that objects in the C-OMB, Hilda, and Trojan populations have comet-like bulk densities of 1 g cm⁻³. This value was selected to roughly split the difference between the extremes of the above values.

Catastrophic disruption scaling law (Q_D^).* To estimate the Q_D^* function for captured comets, we turned to numerical impact experiment results described in Ref. [19, 20]. Ref. [20] performed SPH simulations of impacts into solid ice (dotted red curve in Fig. 3), while Ref. [19] performed CTH simulations into what they describe as ‘weak ice’ (green curve in Fig. 3). The true Q_D^* function should lie between these two extremes (S. Stewart-Mukhopadhyay, personal communication). Thus, we performed simulations where we employ the Ref. [20] strong ice Q_D^* function divided by a factor, f_Q . In order to cover the likely range, we performed three series of simulations, with $f_Q = 3, 5,$ and 8 (see Fig. 3). As a control, we also performed a series with $f_Q = 1$.

Dynamical Evolution. The dynamical evolution of the captured comet population in the main belt (C-OMB), Hilda, and Trojan populations are shown in Fig. 2.

Size-frequency distribution. As a reasonable approximation, we assumed the shape of the initial SFD for all the captured populations resembled that of the observed Trojans. We used this SFD because we believe that the Trojans have only experienced a limited degree of collisional evolution over the last 4 Gy.

The cumulative number $N(> D)$ of known Trojans (from the “astorb.dat” database described above) is well fit by a broken power law with $D^{-5.5}$ for $D > 105$ km, and $D^{-1.8}$ for $D < 105$ km. To normalize this SFD, we followed the power law slope of the $D > 105$ km objects. This trend predicts there should be 1 object with $D > 180$ km. This value was then multiplied by an additional factor 1.1 to roughly account for the estimated amount of comminution experienced by the Trojans over the last 4 Gy.

With the Trojan SFD complete, we can finally take advantage of the dynamical data described in the main text to get the C-OMB population. Numerical integration results suggest that a factor of 4.9 more test bodies were captured in the OMB than in the Trojan L_4 and L_5 regions. In addition, the long-term orbital integrations (§S1) show that the original population is dynamically unstable and drops by a factor of 2.5 over its history. This means the initial C-OMB SFD should be the Trojan population multiplied by a factor $4.9 \times 2.5 = 12.3$. Using a similar argument, we assume the stable Hilda SFD was the same as the initial Trojan SFD multiplied by a factor 6 — a factor of 10 is due to their long-term dynamical behavior, and a factor of 0.6 to account for their different capture probability.

S3. The Micrometeorite Origin Problem

Micrometeorites (MMs) with diameter $D \approx 100\text{--}200 \mu\text{m}$ dominate the present-day flux of extraterrestrial material reaching Earth [44]. MMs are usually classified according to the extent of atmospheric heating they endure (e.g., [45]). Cosmic spherules are fully melted objects. Scoriaeous micrometeorites are unmelted though thermally metamorphosed objects, while fine-grained MMs and coarse-grained MMs are unmelted objects which can be distinguished on the basis of their mean grain size [46]. We exclude cosmic spherules from our discussion since their original texture and mineralogy has been erased by atmospheric entry.

Based on bulk composition, carbon content, and the composition of isolated olivine and pyroxene grains, fine-grained micrometeorites [46] and scoriaeous micrometeorites, which appear to be thermally metamorphosed fine-grained micrometeorites [46, 45, 47], are likely related to carbonaceous chondrites. There is a debate in the literature, however, concerning the origin of the coarse-grained micrometeorites. Ref.[45] and Ref. [48] argued that most coarse-grained micrometeorites were related to carbonaceous chondrites. On the other hand, in a detailed study of the minor element composition, Ref. [24] concluded that 70% of coarse-grained micrometeorites are actually related to ordinary chondrites. Since coarse-grained micrometeorites represent only 20% of the total population, the ratio of ordinary chondrite-type material to carbonaceous chondrite material (hereafter O/C) in MMs is $\lesssim 0.16$.

This stands in stark contrast to the terrestrial meteorite collection, which is dominated by ordinary chondrites [49]. It has been suggested, however, that the different dynamical pathways followed by meteorites and micrometeorites could explain this difference (e.g., Ref [47]). In particular, meteorites sample the ordinary chondrite rich IMB, while MMs should sample the whole MB more uniformly because they evolve inward by radiation forces [50]. Based on the Sloan Digital Sky Survey [51] we estimate that the O/C ratio expected from a uniform sampling of the asteroid belt is 0.7, assuming that carbonaceous chondrites are derived from C-type and D/P-type asteroids, while ordinary chondrites come from S-types (cf. Ref. [49]). If we attempt to correct for contributions from the sources of the known IRAS dust bands, which are due to the recent formation of the Veritas (C-type), Karin (S-type), Beagle (C-type) asteroid families [52, 53, 54], we find that the

expected O/C can be as small as 0.4, but no smaller.

A possible solution to the O/C discrepancy could be that about 2/3 of the collected micrometeorites are produced by comets when they are active during their transits of the inner Solar System. The problem with this solution is that cometary particles typically encounter the Earth at large velocities, so that they either burn up in the atmosphere or are converted into cosmic spherules. As we said at the beginning of §S3, we have not been considering cosmic spherules because they are highly processed. Thus, it is unlikely that a large contribution of MMs from active comets can explain the O/C discrepancy.

We believe that the work presented in this paper provides a more realistic explanation. In particular, we have shown that a very large population of cometary bodies, which formed outside of ~ 15 AU, was implanted in the outer asteroid belt. This population far outnumbered that of the indigenous asteroids at the end of planetary migration. In order to reconcile this result with the fact that the most likely objects of cometary origin, the D-type and P-type asteroids, constitute only a few tens of percent of the outer main belt population, we had to assume that the implanted objects are very fragile, and therefore underwent collisional comminution more effectively than the indigenous S-type or C-type asteroids. With this assumption, which is supported by recent hydrocode impact simulations [19], we were able to match the size distribution and the relative proportions of Trojans, Hildas, and main belt D- and P-type objects. The implication of this effective grinding is that, at the present time, the implanted population is producing a significantly larger fraction of MMs than its overall numbers would suggest.

To show this quantitatively, we need to compute the fraction of small particles created by the C-OMB (pop. 3) versus that of the rest of the asteroid belt combined (IMB and OMB; pop. 1-2). We accomplish this by performing a series of collisional grinding simulations of systems consisting of the IMB, the I-OMB, and the C-OMB. Since we are interested in the current epoch, we assume that the IMB and the OMB have their current SFDs (see §S2.1), and set the C-OMB to be a fixed fraction (f_C) of the OMB at all sizes. We performed simulations for $f_C = 0.2$ and 0.3 , and $f_Q = 3, 5, \text{ and } 8$. We then used CoDDEM to track the collisional evolution of three populations for 10 My. For each f_C and f_Q pair, we performed 100 simulations, each with different random seeds.

We found that the O/C ratio of MMs in our simulations significantly varies from run to run because the amount of MMs produced in each population is strongly dependent on the largest object to undergo a major collision. Thus, we can only analyze our runs statistically. We find that the median value of O/C ranges from 0.09 to 0.26 depending on the values of f_C and f_Q . The series of runs that produced the best O/C was for $f_C = 0.3$ and $f_Q = 8$, which were the runs with the largest number of D-types that were at their weakest. Perhaps most importantly, in all six series, there are a significant fraction of simulations for which $O/C < 0.16$, which is what is needed to solve the MM problem.

There are two lines of experimental evidence that support the idea that the bulk of the MMs are associated with primitive objects embedded in the main belt (e.g., D/P-type). A recent study

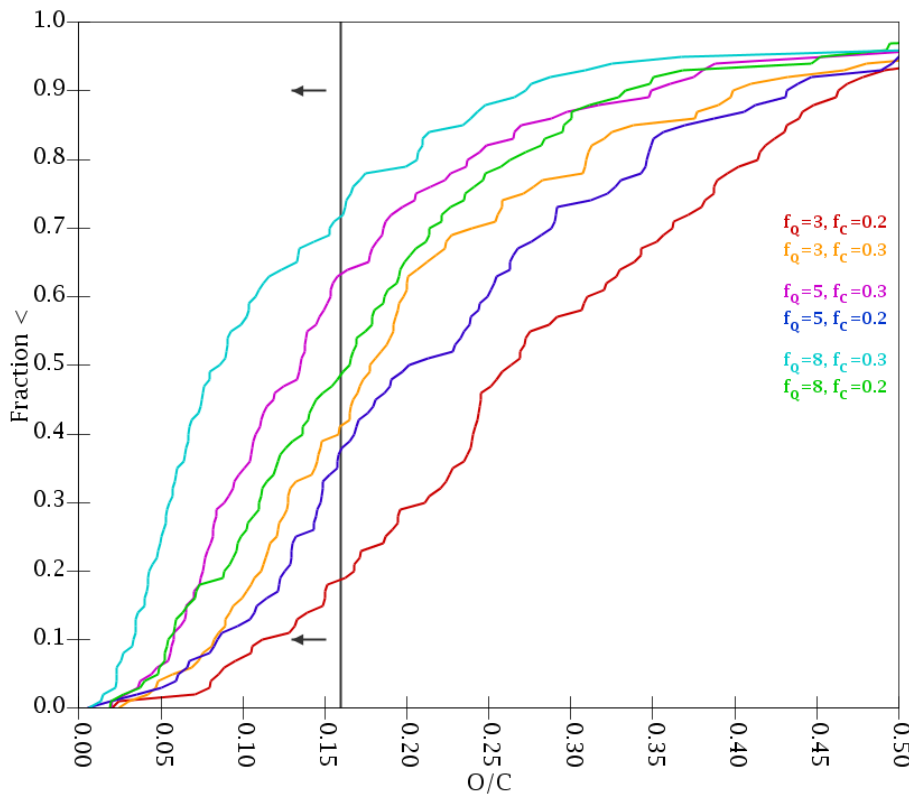


Fig. 4.— The cumulative O/C distribution of unmelted MMs (i.e., the ratio of ordinary chondrite-type MMs to carbonaceous chondrite-type MMs) generated from six series of simulations with different values of f_C and f_Q (see text). To generate these data, we assume that the number of MMs generated in each simulation is proportional to the total change in the volume of all $D > 20$ km asteroids. The black line denotes the observed value $O/C \lesssim 0.16$.

of the synchrotron X-ray diffraction patterns and transmission electron microscopy of four pristine fine-grained micrometeorites concluded that three of them had similar mineralogy to the Tagish Lake meteorite. Given that Tagish Lake is a rare type of chondrite that has a similar spectra to D-type asteroids [55], the link between MMs and Tagish Lake establishes a connection between MMs and the implanted cometary objects.

Oxygen isotopes can also be used in this regard. Recently, Matrajt and collaborators [5] measured the oxygen isotopic composition of 28 unmelted MMs (fine-grained, scoriaceous and coarse-grained MMs). Most of them fall along the same fractionation line as CI meteorites and Tagish Lake (i.e. the terrestrial fractionation line; see Figure 5) but on a different line than the CM meteorites, which are linked with C-type asteroids (e.g., [22, 23]) and different from ordinary chondrite (OCS in the figure), which are associated with S-types. This strongly supports the connection between the MMs and the D-types asteroids. (The parent bodies of CI chondrites are still debated, though Orgueil has been linked to an orbit frequented by Jupiter-family comets; [56]).

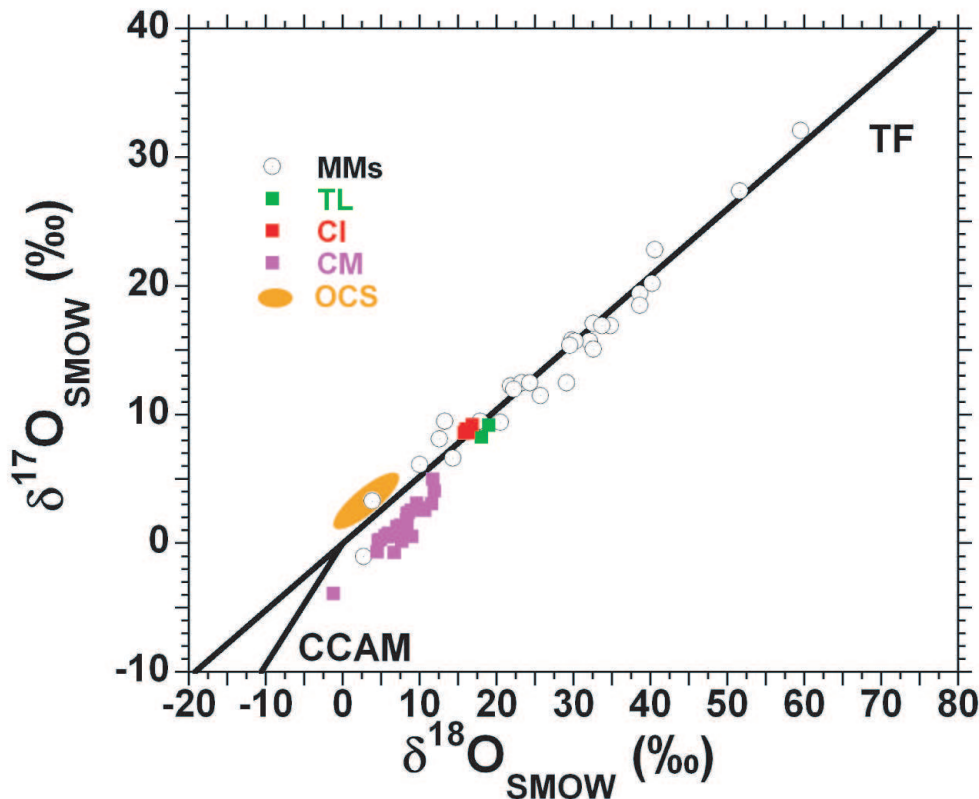


Fig. 5.— The oxygen isotopic composition of micrometeorites compared to that of related groups of chondrites (ordinary chondrites, OCS, and the carbonaceous chondrites CMS, CIS, and Tagish Lake). Other chondrite groups, such as enstatite chondrites are not taken into account in this plot because extensive chemical, petrographic and mineralogical studies of MMS have demonstrated that MMs are exclusively related to the aforementioned groups (e.g., Ref. [46]). Enstatite chondrites are metal-rich, extremely reduced chondrites which are radically different from the metal-poor, oxidized MMs. The oxygen isotopic composition is given using the δ notation, i.e. $\delta^{17,18}\text{O} = ((^{17,18}\text{O}/^{16}\text{O})_{\text{sample}} / (^{17,18}\text{O}/^{16}\text{O})_{\text{SMOW}} - 1) \times 1000$. The terrestrial standard mean ocean water (SMOW) compositions are: $^{17}\text{O}/^{16}\text{O} = 3.8288 \times 10^{-4}$ and $^{18}\text{O}/^{16}\text{O} = 2.0052 \times 10^{-3}$, respectively. The Carbonaceous Chondritic Anhydrous Minerals (CCAM) line is defined by refractory minerals in primitive chondritic meteorites [6]. The terrestrial fractionation line (TF) is defined by measurements of terrestrial and lunar minerals. Micrometeorites' data are from [5]. Data for ordinary, CM and CI chondrites are from Ref. [6]. Data for Tagish Lake (TL) are from Ref. [57].

S4. The Collisional Evolution of the Primordial Cometary Disk.

The dynamical evolution of the planets in the Nice model requires that the trans-Neptunian disk contained 25–35 Earth masses of material at the time when the giant planets became unstable

[2, 4]. Thus, in a scenario where this instability is related to the origin of the LHB [4], the primordial cometary disk must have contained this amount of material after 600 My of collisional grinding. Here, we check whether the values of f_Q that we adopt in our main calculations are consistent with this constraint. For this purpose, we employed `Boulder` [15], a statistical coagulation/fragmentation code of the collisional accretion process constructed along the lines of previous codes (e.g., [58, 59, 60]). In addition to Q_D^* , we need to specify the SFD and the dynamical state of the disk in order to perform these calculations.

Analyzing the current SFDs of the Kuiper belt and Jupiter’s Trojans, Ref. [35] deduced that the cometary disk’s SFD had to be different in its inner and outer regions (see also [8]). The inner part contained 500-1,000 Pluto-size bodies and its SFD had $N(> D) \propto D^{-3}$ for $D > 100$ km and $\propto D^{-2}$ for smaller sizes (dashed red curve in Fig. 6). The outer disk followed the SFD described in §2.2, and was scaled so there was one Pluto-sized object (dashed green curve). As a result, the disk initially contained $60 M_\oplus$.

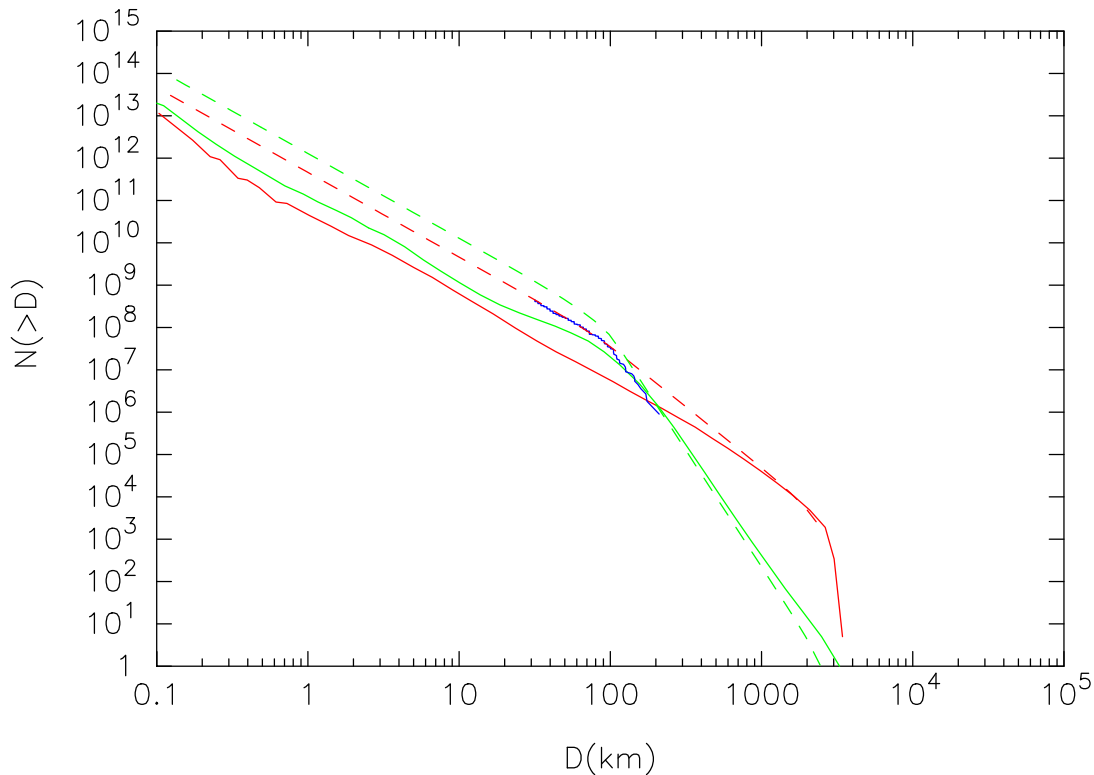


Fig. 6.— Collisional evolution in the trans-Neptunian disk. The dashed lines show our assumed initial SFDs. Red refers to the inner disk and green to the outer disk. With the same color code, the solid lines show the final SFDs after 600 My of collisional grinding, with $f_Q = 3$. The blue curve shows the current SFD of the Trojan objects, scaled to match the number of objects larger than $D = 150$ km in the final SFD of the outer disk.

We used the simulations in Ref. [4] to estimate the dynamical state of the disk. At 300 My (i.e. halfway to the LHB event), the disk has a sharp divide at the location of Neptune’s 1:2 MMR;

the inner part being more excited by the planets. For simplicity sake we assumed that the region interior to the 1:2 MMR contained the inner disk SFD, while the outer disk SFD was beyond this resonance. Given this geometry and SFDs, we estimated the effects of self-stirring in each region. For our collisional simulations, we took the maximum of the self-stirring and the excitation observed in Ref. [4]'s simulation. So, we adopted a mean impact velocity among inner disk particles of 0.83 km/s, with an intrinsic collision probability of $3.8 \times 10^{-21} \text{ km}^{-2} \text{ yr}^{-1}$. The corresponding values for collisions among outer disk particles are 0.25 km/s and $2.5 \times 10^{-21} \text{ km}^{-2} \text{ yr}^{-1}$. For inner-disk/outer-disk collisions we used 0.68 km/s and $4.2 \times 10^{-22} \text{ km}^{-2} \text{ yr}^{-1}$.

Assuming $f_Q = 3$, we find that the disk decays to $25 M_\oplus$ in 600 My. This result is consistent with the amount of mass needed in the Nice-model disk. The final SFDs of the inner and outer disk populations are shown by solid curves in Fig. 6. The two distributions cross over at $D \sim 200 \text{ km}$, as advocated by Ref. [35]. In addition, the SFD of the Trojan asteroids matches the combined distribution as required. Conversely, the simulations assuming $f_Q = 5$ and $f_Q = 8$ give final disks (21 and $18 M_\oplus$, respectively) that are slightly less than the Nice model's nominal value. Also, the slope of the SFD in the 100-300 km range becomes progressively shallower with increasing f_Q and therefore begins to deviate from the Trojan's SFD slope. In summary, the primordial cometary disk constraint suggests low f_Q values, mostly with $f_Q \lesssim 3$, although given the uncertainties of all these calculations, $f_Q \sim 5$ cannot be excluded.

REFERENCES

- [31] Duncan, M. J., Levison, H. F., & Lee, M. H. A multiple time step symplectic algorithm for integrating close encounters. *AJ* **116**, 2067-2077 (1998).
- [32] Wisdom, J., Holman, M. Symplectic maps for the n-body problem. *AJ* **102**, 1528-1538 (1991).
- [33] Durda, D. D., W. F. Bottke, B. L. Enke, E. Asphaug, D. C. Richardson, and Z. M. Leinhardt. The formation of asteroid satellites in catastrophic impacts: Results from numerical simulations. *Icarus* **167**, 382-396 (2004).
- [34] Durda, D., W. F. Bottke, D. Nesvorný, B. Encke, W.J. Merline, E. Asphaug, and D. C. Richardson. Size-Frequency Distributions of Fragments from SPH/N-Body Simulations of Asteroid Impacts. Comparison with Observed Asteroid Families. *Icarus* **186**, 498-516 (2007).
- [35] Morbidelli, A., Levison, H. F., Bottke, W. F., Dones, L., and Nesvorný, D. Considerations on the magnitude distributions of the Kuiper belt and of the Jupiter Trojans. *Icarus*, in press. (2009).
- [36] Bottke, W. F., Nolan, M. C., Greenberg, R., Kolvoord, R. A. Velocity distributions among colliding asteroids. *Icarus* **107**, 255-268 (1994).
- [37] Britt, D. T., Yeomans, D., Housen, K., & Consolmagno, G. Asteroid density, porosity, and structure. In *Asteroids III*, Arizona Press, pp. 485-500 (2002).
- [38] Fowler, J. W., & Chillemi, J. R. IRAS asteroid data processing. In *The IRAS Minor Planet Survey*, Phillips Laboratory, Hanscom AFB, MA, pp. 17-43 (1992).
- [39] Pravec, P., & Harris, A. W. Binary asteroid population. *Icarus* **190**, 250-259 (2007).
- [40] Strom, R. G., Malhotra, R., Ito, T., Yoshida, F., & Kring, D. A. The origin of planetary impactors in the inner Solar System. *Science* **309**, 1847-1850 (2005).
- [41] Dahlgren, M. A study of Hilda asteroids. III. Collision velocities and collision frequencies of Hilda asteroids. *Astron. Astroph.* **336**, 1056-1064 (1998).
- [42] Noll, K. S., Levison, H. F., Grundy, W. M., & Stephens, D. C. Discovery of a binary Centaur. *Icarus* **184**, 611-618 (2006).
- [43] Lacerda, P., Jewitt, D. C. Densities of Solar System objects from their rotational light curves. *AJ* **133**, 1393 (2007).
- [44] Love, S. G., & Brownlee, D. E. A direct measurement of the terrestrial mass accretion rate of cosmic dust. *Science* **262**, 550 (1993).

- [45] Kurat, G., Koeberl, C., Presper, T., Brandstätter, F., & Maurette, M. Petrology and geochemistry of Antarctic micrometeorites. *Geochimica et Cosmochimica Acta* **58**, 3879-3904 (1994).
- [46] Engrand, C., & Maurette, M. Carbonaceous micrometeorites from Antarctica. *Meteoritics and Planetary Science* **33**, 565-580 (1998).
- [47] Genge, M. J., Grady, & M. M., Hutchison, R. The textures and compositions of fine-grained Antarctic micrometeorites - Implications for comparisons with meteorites. *Geochimica et Cosmochimica Acta* **61**, 5149 (1997).
- [48] Engrand, C., Deloule, E., Robert, F., Maurette, M., & Kurat, G. Extraterrestrial water in micrometeorites and cosmic spherules from Antarctica: an ion microprobe study. *Meteoritics and Planetary Science* **34**, 773-786 (1999).
- [49] Meibom, A., & Clark, B. E. Invited review: Evidence for the insignificance of ordinary chondritic material in the asteroid belt. *Meteoritics and Planetary Science* **34**, 7-24 (1999).
- [50] Burns, J. A., Lamy, P. L., Soter, S. Radiation forces on small particles in the solar system. *Icarus* **40**, 1-48 (1979).
- [51] Ivezić, Ž., and 32 colleagues Solar System Objects Observed in the Sloan Digital Sky Survey Commissioning Data. *Astron. J.* **122**, 2749-2784 (2001).
- [52] Nesvorný, D., Bottke, W.F., Levison, H. F., & Dones L. 2003. Recent origin of the Solar System dust bands. *Astrophys. J.* **591**, 486-497 (2003).
- [53] Nesvorný, D., Vokrouhlický, D., Bottke, W. F., & Sykes, M. Physical properties of asteroid dust bands and their sources. *Icarus* **181**, 107-144 (2006).
- [54] Nesvorný, D., Bottke, W. F., Vokrouhlický, D., Sykes, M., Lien, D. J., Stansberry, J. Origin of the Near-Ecliptic Circumsolar Dust Band. *Astrophysical Journal* **679**, L143-L146 (2008).
- [55] Hiroi, T., Zolensky, M. E., & Pieters, C. M. The Tagish Lake meteorite: a possible sample from a D-type asteroid. *Science* **293**, 2234-2236 (2001).
- [56] Gounelle, M., Spurný, P., Bland, P. A. The orbit and atmospheric trajectory of the Orgueil meteorite from historical records. *Meteoritics and Planetary Science* **41**, 135-150 (2006).
- [57] Brown, P. G., & 21 colleagues. The fall, recovery, orbit, and composition of the Tagish Lake meteorite: A new type of carbonaceous chondrite. *Science* **290**, 320-325 (2000).
- [58] Wetherill, G. W., Stewart, G. R. Formation of planetary embryos - Effects of fragmentation, low relative velocity, and independent variation of eccentricity and inclination. *Icarus* **106**, 190 (1993).

- [59] Kenyon, S. J., Luu, J. X. Accretion in the Early Outer Solar System. *Astrophysical Journal* 526, 465-470 (1999).
- [60] Kenyon, S. J., Bromley, B. C. Gravitational Stirring in Planetary Debris Disks. *Astronomical Journal* 121, 538-551 (2001).

This preprint was prepared with the AAS L^AT_EX macros v5.2.